doi:10.1038/nature21677

Star formation inside a galactic outflow

R. Maiolino[1,2], H. R. Russell[3], A. C. Fabian[3], S. Carniani[1,2], R. Gallagher[1,2], S. Cazzoli[4], S. Arribas[4], F. Belfiore[1,2], E. Bellocchi[4], L. Colina[4], G. Cresci[5], W. Ishibashi[6], A. Marconi[5,7], F. Mannucci[5], E. Oliva[5] & E. Sturm[8]

Recent observations have revealed massive galactic molecular outflows[1–3] that may have the physical conditions (high gas densities[4–6]) required to form stars. Indeed, several recent models predict that such massive outflows may ignite star formation within the outflow itself[7–11]. This star-formation mode, in which stars form with high radial velocities, could contribute to the morphological evolution of galaxies[12], to the evolution in size and velocity dispersion of the spheroidal component of galaxies[11,13], and would contribute to the population of high-velocity stars, which could even escape the galaxy[13]. Such star formation could provide *in situ* chemical enrichment of the circumgalactic and intergalactic medium (through supernova explosions of young stars on large orbits), and some models also predict it to contribute substantially to the star-formation rate observed in distant galaxies[9]. Although there exists observational evidence for star formation triggered by outflows or jets into their host galaxy, as a consequence of gas compression, evidence for star formation occurring within galactic outflows is still missing. Here we report spectroscopic observations that unambiguously reveal star formation occurring in a galactic outflow at a redshift of 0.0448. The inferred star-formation rate in the outflow is larger than 15 solar masses per year. Star formation may also be occurring in other galactic outflows, but may have been missed by previous observations owing to the lack of adequate diagnostics[14,15].

IRAS F23128−5919 is a merging system (Fig. 1a), in which the southern nucleus hosts an obscured active galactic nucleus (AGN), detected in the X-rays[16]. Past observations had already revealed a prominent outflow developing from the southern nucleus[14,15,17–19], driven by the nuclear starburst, or by the AGN, or both. We analysed archival Very Large Telescope (VLT) spectroscopic observations, obtained with the MUSE instrument, of the optical nebular lines to characterize the outflow better. The nebular emission line profiles can be separated clearly into a narrow component, associated with the interstellar medium in the two galactic disks, and a very broad (full-width at half-maximum, FWHM $\approx$ 600–1,000 km s^{-1}), predominantly blueshifted component tracing the outflow. The velocity field, velocity dispersion and surface brightness maps of the two components are shown in Fig. 1a. The narrow component (bottom row in Fig. 1a) is probably tracing the bulk of the dynamics of the two merging disks. The outflow traced by the broad blueshifted component (top row in Fig. 1a) of the nebular lines extends towards the East of the southern nucleus for about 7–9 kiloparsecs (8″–10″), beyond the optical galactic disk. A receding counter-outflow is also observed in the opposite direction, that is, towards the West (although it is weaker, owing to extinction by the galactic disk).

We have observed the central and eastern outflows with the X-shooter spectrograph at the VLT, which enabled the detection of spectral diagnostics over the entire spectral range from 0.35 μm to 2.5 μm, and with a spectral resolution and sensitivity higher than the MUSE data. The slit location (box) is shown in Fig. 1a. An example of a spectrum extracted from the central region is shown in Fig. 1b, zoomed around some of the relevant emission lines. The high spectral resolution and high sensitivity of the X-shooter spectra reveal that at least two or three Gaussian components are needed to properly reproduce the asymmetric profile of the broad component of the nebular emission lines, in addition to the narrow component tracing the interstellar medium in the host galaxy (see Methods). We will, however, show that the results do not depend critically on the Gaussian decomposition.

Figure 2a shows the location of the various emission-line components tracing the outflow onto the so-called 'BPT diagnostic diagrams', which are widely used to obtain an approximate discrimination between different excitation mechanisms[20]. Most components describing the outflow (broad blueshifted components) are located in the region of the diagram populated by star-forming galaxies and H II regions, with only a few exceptions mostly restricted to the diagram involving the [N II] line; however, this diagnostic has potential problems associated with the nitrogen abundance[21,22] and, in this specific target, the [N II] line is also affected by telluric absorption, whose correction introduces additional uncertainties.

The finding that nebular components tracing the outflow are located in the star-forming locus of the BPT diagrams provides a first indication that star formation is probably occurring in the outflow. However, the BPT diagrams do not necessarily provide an unambiguous classification. For instance, there are excitation models that predict that some shocks could produce line ratios in the 'star-forming' region of the BPT diagrams[23].

Fortunately, the X-shooter wide spectral range provides a wealth of additional diagnostics of the excitation mechanism. Shock/AGN excitation can be cleanly distinguished from excitation by young stars in the [Fe II] $\lambda = 1.64$ μm/Brγ $\lambda = 2.16$ μm versus the H_2(1–0)S(1) $\lambda = 2.12$ μm/Brγ diagram[24], as shown in Fig. 2b (see Methods for details). Blue symbols indicate the line ratios of the components tracing the central part of the outflow in IRAS F23128−5919, indicating that the gas excitation in the outflow is consistent with star formation and not consistent with other excitation mechanisms, such as shocks or AGNs. The [Fe II] $\lambda = 1.25$ μm/Paβ versus [P II] $\lambda = 1.18$ μm/Paβ diagram is also a good discriminator of the excitation mechanism[25], as illustrated in Fig. 2c. The outflow in IRAS F23128−5919 is inconsistent either with shock excitation or with AGN photoionization. The outflow line ratios are consistent with those observed in star-forming galaxies.

As illustrated in Fig. 1b, the spectrum of IRAS F23128−5919 does not show evidence for coronal lines, which are generally associated with powerful AGNs. This further supports the absence of a substantial AGN contribution to the gas excitation (see Methods for further discussion). Therefore, neither shocks nor the AGN can account for the excitation of the gas in the outflow, whereas all diagnostics are consistent with excitation by star formation.

The presence of young stars is clearly revealed in the ultraviolet Hubble Space Telescope (HST) images (Fig. 1a). However, from imaging alone it is not possible to disentangle putative young stars in the outflow from young stars in the galaxy disks, whose ultraviolet radiation field

[1]Cavendish Laboratory, University of Cambridge, 19 J. J. Thomson Avenue, Cambridge CB3 0HE, UK. [2]Kavli Institute for Cosmology, University of Cambridge, Madingley Road, Cambridge CB3 0HA, UK. [3]Institute of Astronomy, Madingley Road, Cambridge CB3 0HA, UK. [4]CSIC—Departamento de Astrofisica—Centro de Astrobiologia (CSIC-INTA), Torrejon de Ardoz, Madrid, Spain. [5]INAF—Osservatorio Astrofisico di Arcetri, Largo E. Fermi 5, 20125 Firenze, Italy. [6]Physik-Institut, Universität Zürich, Winterthurerstrasse 190, 8057 Zürich, Switzerland. [7]Dipartimento di Fisica e Astronomia, Università degli Studi di Firenze, Via G. Sansone 1, 50019 Sesto F.no, Firenze, Italy. [8]Max-Planck-Institut für Extraterrestrische Physik, Giessenbachstrasse, D-85748 Garching, Germany.

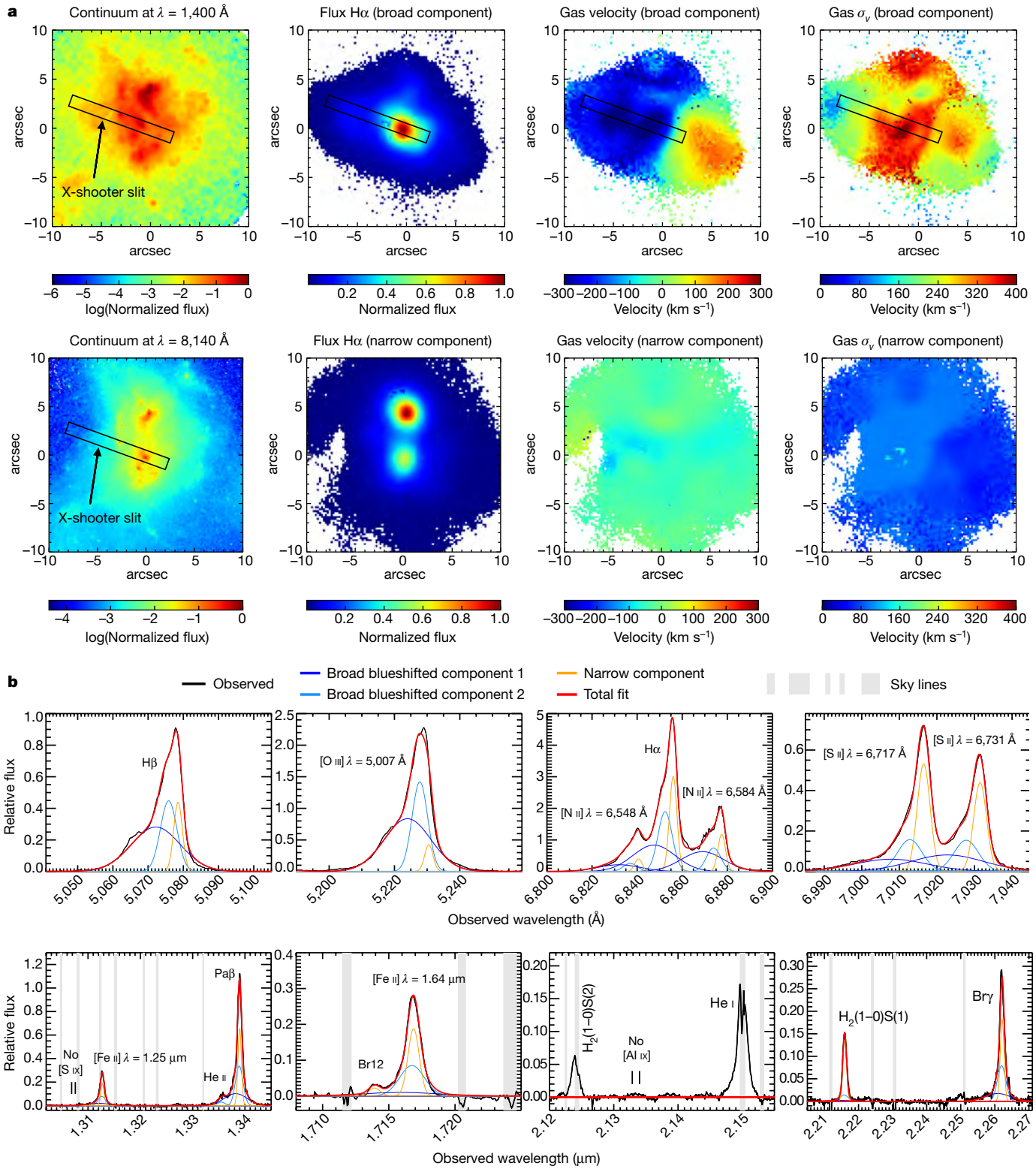

Figure 1 | Spectral decomposition of the outflow in IRAS F23128−5919. **a**, HST continuum images, surface brightness (flux per surface area), velocity and velocity dispersion σ_v maps of the broad and narrow components of the Hα line, inferred from the MUSE data. The location and orientation of the X-shooter slit is shown (boxes). **b**, Subsections of continuum-subtracted X-shooter spectra, extracted from the central region, around some of the relevant emission lines, showing the decomposition between narrow and broad components, as well as the non-detection of coronal lines (see Methods).

can potentially ionize the gas in the outflow (externally) and produce the line ratios observed in the outflow. However, an external source of stellar ionization should result in an ionization parameter (defined as the ratio between ionizing photon flux and gas density; when divided by the speed of light it is the adimensional ionization parameter U) much lower than typically observed in star-forming galaxies. Yet, despite the gas density in the outflow (about 600–1,500 cm^{-3}, as inferred from the [S II] doublet) being higher than in the host galaxy and higher than that typically seen in star-forming galaxies, the ionization parameter of the gas in the outflow, as inferred from the [O III] $\lambda = 5{,}007$ Å/[O II]

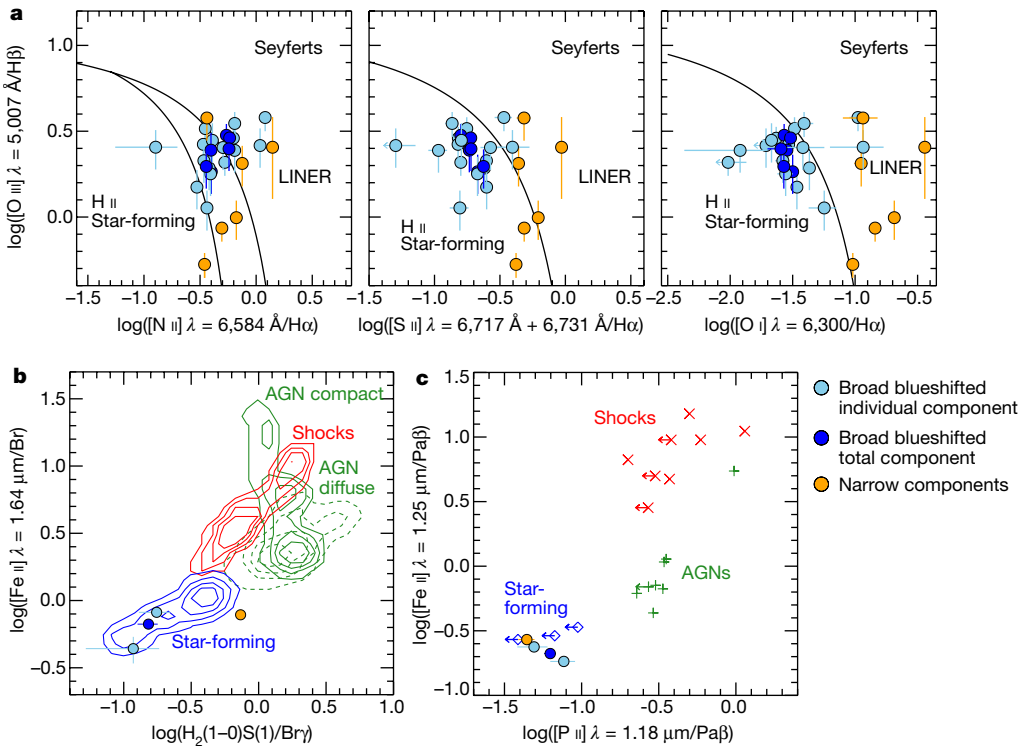

Figure 2 | Diagnostic diagrams. Distributions of the individual broad Gaussians (light-blue symbols) and of the resulting total broad components (dark-blue symbols) tracing the outflow, as well as of the narrow components (orange symbols) tracing gas in the host galaxy, extracted from different apertures along the X-shooter slit. **a**, BPT diagnostic diagrams involving optical nebular lines, showing the dividing curves between H II star-forming regions, Seyferts, and low-ionization nuclear-emitting regions (LINERs)[20,29]. **b**, Diagnostic diagram involving near-infrared nebular lines showing the comparison with the distribution of star-forming galaxies, shocked regions, AGN compact regions and AGN diffuse emission[24]. **c**, Diagnostic diagram based on other infrared emission lines, also showing the comparison with the distribution of various classes of sources. Error bars show the 1σ uncertainties.

$\lambda = 3{,}727$ Å line ratio, is not lower than observed in normal star-forming regions, and is in fact slightly larger, as illustrated in Fig. 3. This result strongly argues in favour of *in situ* stellar photoionization, by young stars within the outflow.

Even better evidence for stars formed in the outflow is the direct detection of a young stellar population with the kinematical fingerprints of formation inside the outflow. The stellar continuum is detected in the X-shooter spectra out to about 5 kpc from the nucleus, and its shape and stellar features do indeed indicate the presence of a young stellar population younger than a few tens of millions of years (Myr). Determining the kinematics of such a stellar population is difficult, since most stellar features (especially the ones associated with young stars) are heavily contaminated by the strong nebular emission lines. However, we have recovered the kinematics of the young stellar populations through our spectral fitting of the optical spectrum (Fig. 4a and Methods), which is dominated by the Balmer lines (tracing young hot O-B-type stars, but also contaminated by older A-type stars) and through the Ca II triplet (CaT) at wavelength $\lambda \approx 8{,}500$ Å (which, in the case of recent star formation, is dominated by young red supergiants and young asymptotic giant branch stars, although the latter are also contributed by older stellar populations). Moreover, we have detected (only in the regions of highest signal-to-noise ratio) the weak absorption feature of He I $\lambda = 4{,}922$ Å (Fig. 4a), which is an unambiguous tracer of B-type stars and of stellar populations with age[26] of about 10 Myr. Figure 4b shows the kinematics of the various components as a function of galactocentric distance along the X-shooter slit. Except for the central kiloparsec, where stellar features are probably dominated by the central starburst in the host galaxy, all stellar features in the outflow region, at a galactocentric radius of about 1–3 kpc, show a blueshift relative to the galactic disk (see Methods for the identification of the latter), indicating that they are indeed associated with

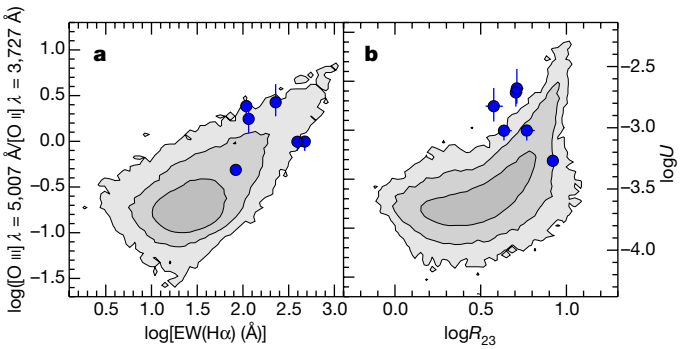

Figure 3 | Ionization parameter. The [O III]/[O II] line ratio (left-hand *y* axis) is sensitive to the adimensional ionization parameter *U*, as given on the right-hand *y* axis[30] (although it also has a secondary dependence on metallicity). **a**, [O III]/[O II] as a function of equivalent width EW(Hα), which is used as a proxy of the age of the stellar population. Contours indicate the distribution of star-forming galaxies from the Sloan Digital Sky Survey survey (68%, 95% and 99.7% of the population), illustrating that younger systems have higher ionization potential. Symbols indicate the location of the gas in the Eastern outflow (we cannot differentiate between individual broad components since we cannot differentiate the continuum associated with each component), indicating that it is consistent with *in situ* photoionization by young stars. **b**, The [O III]/[O II] line ratio has a function of R_{23} = ([O III] $\lambda = 5{,}007$ Å, 4,940 Å + [O II] $\lambda = 3{,}727$ Å)/Hβ, which is sensitive to the metallicity, with a secondary dependence on ionization parameter. The diagram further supports the idea that the gas excitation in the outflow does not differ substantially from normal star-forming regions and, if anything, the ionization parameter is even higher. Error bars show the 1σ uncertainties.

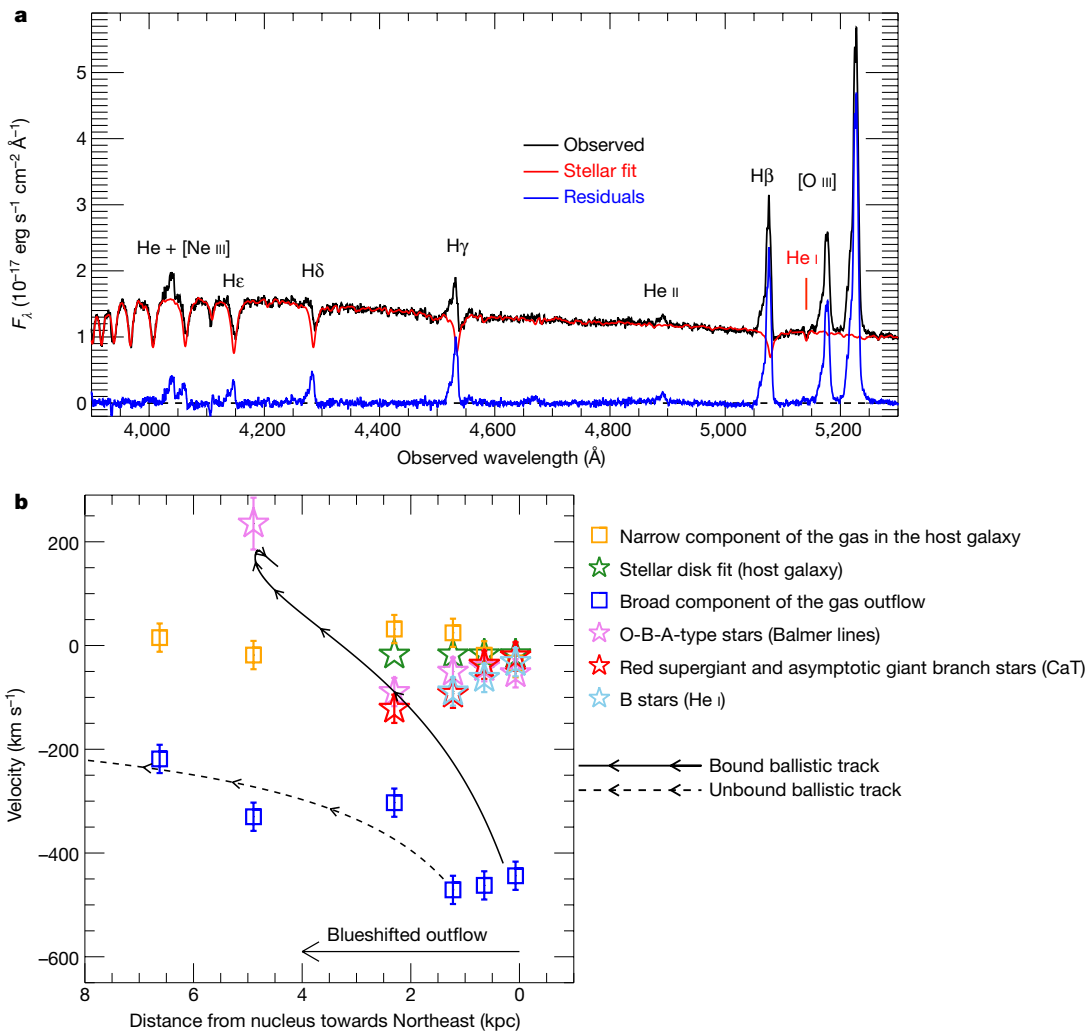

Figure 4 | Kinematics of young stars compared with the gas kinematics. a, Stellar fit of the spectrum extracted from the outflow region at 1 kpc from the nucleus. F_λ is the flux per unit wavelength. **b**, Velocity of the young stellar population along the outflow, traced by different features (see also the Methods) compared with the kinematics of the broad nebular component tracing the gaseous outflow (centroid of the broad Gaussians fitting the broad component; dark-blue symbols), and the kinematics of the host galaxy disk traced by the narrow nebular component (orange symbols) and by a fit of the disk stellar kinematics in the MUSE data (green symbols; see Methods). Black curves show the position–velocity tracks of stars formed in the outflow, according to the model described in the Methods. Error bars show the 1σ uncertainties.

the outflow. The velocity of the stellar features (reaching a maximum blueshift of about 100 km s^{-1}) is much lower than the velocity observed for the nebular lines in the outflow (about 250–450 km s^{-1}); however, this difference is expected in the scenario in which stars form in the outflow.

Indeed, although the gas in the outflow is probably maintained at high velocity (at least in the central 1.5 kpc) by the continuous action of radiation pressure or ram pressure by expanding hot gas, as soon as stars form in the outflow they react only to gravity, and are rapidly decelerated by the galaxy gravitation field (that is, they move ballistically). A simple dynamical model (see Methods) easily describes such an effect. In Fig. 4b the solid curve shows the position–velocity track of stars formed at the base of the outflow (specifically at 500 parsecs from the nucleus, corresponding to a projected distance of about 350 pc), where most of the star formation in the outflow is occurring, as inferred from the broad Hα flux map. Within this model such stars are rapidly decelerated and their velocities even change sign (that is, they fall back towards the disk and towards the bulge), reproducing the positive velocity of young stars observed at 5 kpc from the nucleus. Within this model, stars formed in the outflow at projected distances larger than 1 kpc are only mildly decelerated and become gravitationally unbound (see the dashed curve in Fig. 4b).

Overall, the combined evidence supports the scenario in which stars have formed in the outflow of this galaxy. By using the total Hα emission of the gas in the Eastern (approaching) outflow, and corrected for extinction through the Balmer decrement, we infer a total star-formation rate in the Eastern outflow of about 15 solar masses per year, assuming a 'Chabrier' initial mass function[27]. Performing a similar analysis in the Western (receding) outflow is prevented by the large dust extinction. However, if the Western outflow is also characterized by similar star formation, then the total star-formation rate occurring in the outflow is about 30 solar masses per year, that is, a substantial fraction (about 25%) of the total star-formation rate of the merging system, about 115 solar masses per year[28].

Online Content Methods, along with any additional Extended Data display items and Source Data, are available in the online version of the paper; references unique to these sections appear only in the online paper.

Received 6 September 2016; accepted 25 January 2017.
Published online 27 March 2017.

1. Feruglio, C. *et al.* Quasar feedback revealed by giant molecular outflows. *Astron. Astrophys.* **518,** L155–L158 (2010).
2. Sturm, E. *et al.* Massive molecular outflows and negative feedback in ULIRGs observed by Herschel-PACS. *Astrophys. J.* **733,** L16–L20 (2011).

3. Cicone, C. *et al.* Massive molecular outflows and evidence for AGN feedback from CO observations. *Astron. Astrophys.* **562,** A21–A55 (2014).
4. Aalto, S. *et al.* Detection of HCN, HCO^+, and HNC in the Mrk 231 molecular outflow. Dense molecular gas in the AGN wind. *Astron. Astrophys.* **537,** A44–A51 (2012).
5. Aalto, S. *et al.* High resolution observations of HCN and $HCO^+J=3–2$ in the disk and outflow of Mrk 231. Detection of vibrationally excited HCN in the warped nucleus. *Astron. Astrophys.* **574,** A85–A96 (2015).
6. Sakamoto, K. *et al.* P Cygni profiles of molecular lines toward Arp 220 Nuclei. *Astrophys. J.* **700,** L104–L108 (2009).
7. Ishibashi, W. & Fabian, A. C. Active galactic nucleus feedback and triggering of star formation in galaxies. *Mon. Not. R. Astron. Soc.* **427,** 2998–3005 (2012).
8. Zubovas, K., Nayakshin, S., Sazonov, S. & Sunyaev, R. Outflows of stars due to quasar feedback. *Mon. Not. R. Astron. Soc.* **431,** 793–798 (2013).
9. Silk, J. Unleashing positive feedback: linking the rates of star formation, supermassive black hole accretion, and outflows in distant galaxies. *Astrophys. J.* **772,** 112 (2013).
10. Zubovas, K. & King, A. R. Galaxy-wide outflows: cold gas and star formation at high speeds. *Mon. Not. R. Astron. Soc.* **439,** 400–406 (2014).
11. Ishibashi, W., Fabian, A. C. & Canning, R. E. A. Can AGN feedback-driven star formation explain the size evolution of massive galaxies? *Mon. Not. R. Astron. Soc.* **431,** 2350–2355 (2013).
12. Gaibler, V., Khochfar, S., Krause, M. & Silk, J. Jet-induced star formation in gas-rich galaxies. *Mon. Not. R. Astron. Soc.* **425,** 438–449 (2012).
13. Dugan, Z., Bryan, S., Gaibler, V., Silk, J. & Haas, M. Stellar signatures of AGN-jet-triggered star formation. *Astrophys. J.* **796,** 113 (2014).
14. Leslie, S. K., Rich, J. A., Kewley, L. J. & Dopita, M. A. The energy source and dynamics of infrared luminous galaxy ESO 148–IG002. *Mon. Not. R. Astron. Soc.* **444,** 1842–1853 (2014).
15. Bellocchi, E., Arribas, S., Colina, L. & Miralles-Caballero, D. VLT/VIMOS integral field spectroscopy of luminous and ultraluminous infrared galaxies: 2D kinematic properties. *Astron. Astrophys.* **557,** A59 (2013).
16. Brightman, M. & Nandra, K. An XMM-Newton spectral survey of 12μm selected galaxies—I. X-ray data. *Mon. Not. R. Astron. Soc.* **413,** 1206–1235 (2011).
17. Arribas, S., Colina, L., Bellocchi, E., Maiolino, R. & Villar-Martín, M. Ionized gas outflows and global kinematics of low-z luminous star-forming galaxies. *Astron. Astrophys.* **568,** A14 (2014).
18. Cazzoli, S., Arribas, S., Maiolino, R. & Colina, L. Neutral gas outflows in nearby [U]LIRGs via optical NaD feature. *Astron. Astrophys.* **590,** A125 (2016).
19. Piqueras López, J., Colina, L., Arribas, S., Alonso-Herrero, A. & Bedregal, A. G. VLT-SINFONI integral field spectroscopy of low-z luminous and ultraluminous infrared galaxies. I. Atlas of the 2D gas structure. *Astron. Astrophys.* **546,** A64 (2012).
20. Kewley, L. J., Groves, B., Kauffmann, G. & Heckman, T. The host galaxies and classification of active galactic nuclei. *Mon. Not. R. Astron. Soc.* **372,** 961–976 (2006).
21. Pérez-Montero, E. & Contini, T. The impact of the nitrogen-to-oxygen ratio on ionized nebula diagnostics based on [N ii] emission lines. *Mon. Not. R. Astron. Soc.* **398,** 949–960 (2009).
22. Shapley, A. E. *et al.* The MOSDEF survey: excitation properties of $z\approx2.3$ star-forming galaxies. *Astrophys. J.* **801,** 88 (2015).
23. Allen, M. G., Groves, B. A., Dopita, M. A., Sutherland, R. S. & Kewley, L. J. The MAPPINGS III library of fast radiative shock models. *Astrophys. J. Suppl. Ser.* **178,** 20–55 (2008).
24. Colina, L. *et al.* Understanding the two-dimensional ionization structure in luminous infrared galaxies. A near-IR integral field spectroscopy perspective. *Astron. Astrophys.* **578,** A48 (2015).
25. Oliva, E. *et al.* NICS-TNG infrared spectroscopy of NGC 1068: the first extragalactic measurement of [P ii] and a new tool to constrain the origin of [Fe ii] line emission in galaxies. *Astron. Astrophys.* **369,** L5–L8 (2001).
26. González Delgado, R. M., Cerviño, M., Martins, L. P., Leitherer, C. & Hauschildt, P. H. Evolutionary stellar population synthesis at high spectral resolution: optical wavelengths. *Mon. Not. R. Astron. Soc.* **357,** 945–960 (2005).
27. Kennicutt, R. C. & Evans, N. J. Star formation in the Milky Way and nearby galaxies. *Annu. Rev. Astron. Astrophys.* **50,** 531–608 (2012).
28. Rodríguez-Zaurín, J. *et al.* VLT-VIMOS integral field spectroscopy of luminous and ultraluminous infrared galaxies. III. The atlas of the stellar and ionized gas distribution. *Astron. Astrophys.* **527,** A60 (2011).
29. Kauffmann, G. *et al.* The host galaxies of active galactic nuclei. *Astrophys. J.* **346,** 1055–1077 (2003).
30. Diaz, A. I., Castellanos, M., Terlevich, E. & Luisa Garcia-Vargas, M. Chemical abundances and ionizing clusters of Hii regions in the LINER galaxy NGC 4258. *Mon. Not. R. Astron. Soc.* **318,** 462–474 (2000).

Acknowledgements R.M., S.Car. and F.B. acknowledge support by the Science and Technology Facilities Council (STFC). R.M. acknowledges ERC Advanced Grant 695671 "QUENCH". H.R.R. and A.C.F. acknowledge ERC Advanced Grant 340442. S.A., S.Caz., E.B. and L.C. acknowledge support from the Spanish Ministry of Economy, under grants AYA2012-32295 and ESP2015-68964-P.

Author Contributions R.M. led the project and performed data analysis and interpretation. H.R.R. performed X-shooter data reduction. A.C.F. and W.I. did the theoretical modelling. S.Car., S.A. and E.B. did the reduction and analysis of the MUSE data. S.Caz. and R.G. performed stellar continuum subtraction and continuum analysis. L.C. interpreted the near-infrared spectra. E.O. performed nebular and stellar line identification and diagnostics. F.M., A.M., G.C. and E.S contributed to interpretation. F.B. performed the comparison with Sloan Digital Sky Survey data.

Author Information Reprints and permissions information is available at www.nature.com/reprints. The authors declare no competing financial interests. Readers are welcome to comment on the online version of the paper. Publisher's note: Springer Nature remains neutral with regard to jurisdictional claims in published maps and institutional affiliations. Correspondence and requests for materials should be addressed to R.M. (r.maiolino@mrao.cam.ac.uk).

Reviewer Information *Nature* thanks M. Sarzi, K. Zubovas and the other anonymous reviewer(s) for their contribution to the peer review of this work.

METHODS

Data reduction and analysis. The optical integral field spectroscopic data were retrieved from the European Southern Observatory (ESO) archive and were obtained with the MUSE spectrometer at the ESO's VLT with an on-source integration time of 52 min. The wavelength coverage is from 0.46 μm to 0.93 μm and the spectral resolution varies from $R = 2{,}000$ to $R = 4{,}000$ across the wavelength range. The seeing during the observations was only about 2.5″. The stellar continuum was fitted and subtracted at each pixel by using the PPXF routine[31] by using the MILES templates[32]. The nebular lines Hα, [N II] $\lambda = 6{,}548$ Å, [N II] $\lambda = 6{,}584$ Å, [S II] $\lambda = 6{,}717$ Å, [S II] $\lambda = 6{,}731$ Å, [O I] $\lambda = 6{,}300$ Å, Hβ, [O III] $\lambda = 4{,}959$ Å and [O III] $\lambda = 5{,}007$ Å were simultaneously fitted with two Gaussian components, a narrow one with FWHM $< 300\,\mathrm{km\,s^{-1}}$ and a broad one with FWHM $> 300\,\mathrm{km\,s^{-1}}$. At each spatial position the velocity and velocity dispersion of each of the two components was fixed for all nebular lines. The intensities of the [N II] doublet and of the [O III] doublet were tied to have the ratio given by their Einstein coefficients. The resulting maps of the Hα flux, velocity and velocity dispersion of the two components in Fig. 1a are obtained by masking out regions for which the signal-to-noise ratio of the component is lower than five. We note that in previous work[15], which analysed data of the same source, obtained with the VIMOS instrument at the VLT, the most Eastern nebular emission was associated with the 'narrow' component but fitted with very large velocity dispersion ($\sigma_v \approx 300\,\mathrm{km\,s^{-1}}$) and was very blueshifted (velocity $v < -300\,\mathrm{km\,s^{-1}}$). This mismatch was probably due to the lower signal-to-noise ratio of the VIMOS data in those external regions, which made the line decomposition much more difficult. In our analysis, using MUSE data, we have corrected this (not completely appropriate) association: such high values of the velocity dispersion and strong blueshift should actually be associated with the 'broad' blueshifted component which traces the outflow.

The new spectra were obtained with the spectrometer X-shooter[33] at the ESO's VLT. We selected the 11″-long slit with a width of 1.3″ in the ultraviolet B (UVB) arm (wavelength spectral range 300–560 nm), 1.2″ in the visible (VIS) arm (spectral range 550–1,020 nm) and 1.2″ in the near-infrared (NIR) arm (spectral range 1,020–2,480 nm). The resulting spectral resolutions are $R = 4{,}000$ in the UVB, $R = 6{,}700$ in the VIS and $R = 3{,}890$ in the NIR. The seeing during the observations was about 0.9″ on average. The slit was positioned with a position angle of 70° with the southern nucleus centred at 3.2″ from the centre of the slit (Fig. 1a); this orientation and centring enables the slit to sample both the nuclear and the Eastern part of the outflow. Observations were executed by nodding the slit by a few arcsec (to optimize the removal of detector artefacts) and interleaved with blank sky exposures, obtained at about 1 arcmin from the galaxy, for sampling the background. The total on-source integration time was 1.7 h. Data reduction and calibration was performed following the standard pipeline steps[34]. Great care was taken to correct the atmospheric absorption features, not only in the NIR, but also in the VIS, by using the telluric standard and by smoothing its spectrum to the resolution of the science observations (the spectral resolution of the telluric standard is much higher, by about 30%, than the science observation because the seeing was smaller than the slit).

We extracted six spectra along the slit, with variable apertures (from 0.5″ to 2.5″), to find a trade-off between spatial information and the signal-to-noise ratio. The continuum spectra were fitted with PPXF[31] by using the MILES stellar synthesis library[32]. The whole library was used in the fitting. However, we note that, unfortunately, templates covering the required spectral range at the high resolution of our spectra are available only for ages down to 30 Myr. This constraint implies that we cannot disentangle populations younger than 30 Myr. More specifically, all spectral fits require a population of 30 Myr (jointly with contribution from older stellar populations), but this must be regarded as an upper limit of the youngest stellar population because of the library limits. We adopted two strategies for fitting the continuum: (1) we masked all of the nebular lines (over their whole width, about 30–40 Å) and fitted the remaining portion of the spectrum; (2) we simultaneously fitted the nebular lines (with their multiple velocity components) and the stellar continuum without any masking. The resulting fluxes and decomposition of the nebular lines do not change depending on the method. However, from the simulations, the stellar kinematics (especially the young component associated with the Balmer lines) is better recovered using the second method. The He I emission and absorption line was fitted separately, as this feature may trace a different stellar population with a different kinematics. For this fitting the shape of the He I emission was fixed to that of [O III] $\lambda = 5{,}007$ Å, but allowed to vary in flux. Regarding the fitting of the Ca II triplet (which was fitted independently of the rest of the spectrum), we have restricted it to the bluest of the three lines ($\lambda = 8{,}498$ Å) since the other two lines are heavily affected by sky emission lines and telluric absorption.

The different stellar populations in the stellar fit should in principle be allowed to have different velocities. In particular, we should in principle allow the old stellar population to have a different velocity relative to the young stellar population. However, this is not really possible in practice because: (1) this additional degree of freedom would introduce a lot of degeneracy when also attempting to simultaneously deblend the nebular line emission from the stellar features, and (2) the young stellar population dominates the observed stellar light across the entire spectrum, hence the velocity traced by the spectral features associated with the old stellar population is extremely difficult to recover.

Note that the signal-to-noise ratio in the spectra allows us to trace the stellar kinematics through the He I line only out to 1.2 kpc, and through the Ca II triplet only out to 2.3 kpc. At 5 kpc the stellar kinematics can be recovered only through the Balmer absorption lines. At 6.6 kpc (the outermost point at which the spectrum is extracted) the very low signal-to-noise ratio on the continuum does not allow us to detect stellar signatures.

It is interesting to note that the spectrum extracted at 2.3 kpc (sampling from 2″ to 3.6″ from the nucleus) includes a clear knot observed in the HST image. This could be a star cluster that has formed within the outflow. Indeed, in the position–velocity diagram (Fig. 4b) it is located on the ballistic track of particles formed in the inner part of the outflow.

Regarding the specific fitting of the nebular lines, in the optical spectra, the higher spectral resolution and higher signal-to-noise ratio of the X-shooter data reveals that the broad blueshifted component tracing the outflow cannot be reproduced with a single Gaussian. In the central aperture the broad component requires at least two blueshifted broad Gaussians (blue lines in Fig. 1b) to be properly fitted (along with a narrow component accounting for gas in the host galaxy). In some of the Eastern apertures, dominated by the outflowing gas, the broad blueshifted component requires three Gaussian components to be properly fitted. In the latter apertures a very weak narrow component (even more clearly separated from the broad component), associated with the outskirts of the host galaxy in the background is also always detected.

The fitting of these components in the X-shooter spectra is performed by requiring that the centre and width of each of these components is the same for all nebular lines and that only their amplitudes may vary. For the two nitrogen lines [N II]6548,6584 and the two oxygen lines [O III]4959,5007 their relative intensities was fixed to match the relative values of the Einstein transition coefficients.

In the central aperture, absorption by a diffuse interstellar band at $\lambda = 6{,}282$ Å affects the blue shoulder of the bluest and broadest component of the [O I] $\lambda = 6{,}300$ Å line, so the spectral region in the range 6,125 Å $< \lambda_{\mathrm{rest}} <$ 6,291 Å was not included in the fit. This results in a slightly higher uncertainty of the fit parameters for this component of the [O I] line. For the [O II] $\lambda = 3{,}727$ doublet there is some degeneracy on the fit of the three components tracing the outflow in the eastern spectrum. However, since we do not use the relative intensity of the two lines of the [O II] doublet to infer anything about the gas density, but only their sum to investigate the ionization parameter (along with [O III]), this degeneracy does not affect our results.

The line profiles (for example, Fig. 1b) have clear humps and changes of slope, which leave little ambiguity about the multi-component decomposition of the lines. However, since ascribing a specific physical meaning to each individual broad component is not relevant for this paper, we also combine all broad components together in the diagnostic diagrams of Fig. 2. This may still leave some ambiguity about the decomposition of the broad and narrow components. However, except for the nuclear region, in most of the outflow the line flux is totally dominated by the broad component; hence, even if the narrow component were totally incorporated into the broad component, this would not change the location on the BPT diagrams of Fig. 2.

For the optical nebular lines, we corrected for dust reddening (by using a Milky Way extinction curve[28]) by using the Hβ/Hγ ratio to infer the reddening. Hα/Hβ cannot be used, as these two lines were observed with different apertures.

In the NIR data of the nuclear region (which is the only region where we can extract the spectrum with a signal-to-noise ratio high enough for a proper spectral decomposition), the profile of the nebular lines changes substantially relative to the optical lines. This is primarily due to the effect of differential dust extinction, as a consequence of which some components are much more absorbed in the VIS than in the NIR. Therefore, we fitted the NIR lines separately with a different set of components, not tied to the parameters of the optical components, although the general properties are similar.

In the NIR the diagnostic line ratios are corrected for dust reddening by using a Milky Way extinction curve[35] and by using the Brγ/Paβ ratio to infer the reddening (although the inferred reddening is low and most of these line ratios are in fact unaffected by dust reddening).

Some additional NIR spectral regions of interest are shown in Extended Data Fig. 1. We note that in many cases (especially thanks to the high signal-to-noise ratio of the optical spectrum) the formal errors on the central velocity are very small, both for the gaseous and the stellar features. However, in Fig. 4b we

conservatively give a minimum error bar corresponding to half of the spectral resolution element.

NIR diagnostic diagrams. As the NIR diagnostic diagrams are generally less used (owing to the greater technical/observational difficulties in obtaining NIR spectra with appropriate sensitivity) here we provide some details about their physical meaning and about the way they were obtained.

The NIR iron lines are extremely useful to identify shock excitation. Indeed, shocks are known to destroy dust grains, hence releasing into the interstellar medium large amounts of iron, which is otherwise locked into grains. This results in much higher emission of iron NIR transitions, relative to the hydrogen recombination lines, than is typically observed in star-forming regions. Shock heating of the interstellar medium also results in excitation of the NIR vibrational transition of molecular hydrogen. These are the reasons why the [Fe II] $\lambda = 1.64\,\mu$m/Brγ versus H_2(1–0)S(1) $\lambda = 2.12\,\mu$m/Brγ diagram (Fig. 2b) is so effective in disentangling shocks from star-forming regions, as outlined in ref. 24, from which the distribution of the different classes of excitation sources have been taken.

The low ionization line [P II] $\lambda = 1.18\,\mu$m is an excellent diagnostic of partially ionized, transition regions produced by X-rays, produced either by radiative shocks or by AGNs[25]. The ratios [Fe II] $\lambda = 1.25\,\mu$m/Paβ versus [P II] $\lambda = 1.18\,\mu$m/Paβ shown in Fig. 2c for different classes of objects were obtained from the literature[25,36–38] and illustrate that this diagram is also very effective in disentangling different excitation mechanisms. Note that the comparison with AGNs is limited to the 'type 2' class to avoid contribution to Brγ and Paβ from the broad line region.

Coronal lines. Coronal lines are not detected in our X-shooter spectrum of IRAS F23128−5919. In particular, none of the coronal lines observable in good regions of atmospheric transmission ([S VIII] $\lambda = 0.9913\,\mu$m, [Fe XIII] $\lambda = 1.0747\,\mu$m, [S IX] $\lambda = 1.252\,\mu$m, [Al IX] $\lambda = 2.045\,\mu$m) is detected. Although coronal lines are not always seen in AGNs, most of the powerful AGNs do show evidence for coronal lines in the NIR (which is the wavelength range hosting many of the most intense coronal lines), especially if observed with appropriate signal-to-noise ratio and for those AGNs not suffering dilution from star formation in the host galaxy[36,39–44]. For instance, in the prototypical Sy2 galaxy Ciricinus, [Al IX] $\lambda = 2.045\,\mu$m is three times stronger than the nearby He I $\lambda = 2.058\,\mu$m line[42], while in IRAS F23128−5919 [Al IX] $\lambda = 2.045\,\mu$m is completely undetected (despite being in a region of good atmospheric transmission and unaffected by OH sky lines), implying that it is at least 20 times fainter than the He I $\lambda = 2.058\,\mu$m line (Fig. 1b).

However, previous work[44] has claimed the detection of weak [Si VI] $\lambda = 1.96\,\mu$m emission in IRAS F23128−5919. This line is shifted in a bad region of atmospheric transmission and also plagued by a prominent OH sky line, so it is difficult to assess its presence even with the high signal-to-noise ratio of our spectra. Extended Data Fig. 1b shows the nuclear spectrum of IRAS F23128−5919 extracted from the nuclear aperture, zoomed around the expected location of [Si VI]. The vertical lines indicate the expected location of the three Gaussian components used to fit the nebular lines in the NIR spectrum. Although no features are associated with the narrow and intermediate broad components, there is indeed a weak feature around the expected location of the broadest component. However, the detected feature is much narrower than the expected component at this wavelength. Indeed, if included in the simultaneous fit together with all the other nebular infrared lines, the fitting procedure sets to zero the flux of the putative [Si VI] component associated with the observed feature, because it cannot accommodate the narrow profile of the feature. It could be that this feature represents highly ionized gas ionized by the AGN in the central region of IRAS F23128−5919 that has kinematic properties different from all the other nebular lines. Alternatively, we note that the feature is located exactly at the wavelength of one of the deepest atmospheric features in the K-band, which is very difficult to correct, so the observed feature could be a residual of an imperfect correction of the telluric absorption. However, even if the feature is real and associated with [Si VI], this would simply confirm the presence of the obscured AGN in the southern nucleus of IRAS F23128−5919, but it would not affect our conclusion that the photoionization of the bulk of the gas associated with the broad blueshifted component tracing the outflow is not due to the AGN, both because the observed coronal line is very weak (a factor of 30 weaker than observed in other classical AGNs such as Circinus and NGC1068, relative to Brγ) and because it appears to have different kinematic properties.

He II line detection. It is interesting to note that the He II $\lambda = 4{,}686$ Å line is clearly detected in the outflow, although weak (Fig. 4a). Its intensity relative to Hβ ($F_{\mathrm{He\,II}\lambda=4{,}686\,\text{Å}}/F_{\mathrm{H}\beta} \approx 0.07$) is much lower than observed in the narrow line region of AGNs (for which generally $F_{\mathrm{He\,II}\lambda=4{,}686\,\text{Å}}/F_{\mathrm{H}\beta} \approx 0.3$–$0.5$)[29,43], but it is close to the value observed in very young star-forming galaxies ($F_{\mathrm{He\,II}\lambda=4{,}686\,\text{Å}}/F_{\mathrm{H}\beta} \approx 0.01$–$0.08$)[45,46]. In young star-forming galaxies the weak He II emission is ascribed to excitation by radiative shocks associated with supernovae or stellar winds, which contribute little to the overall ionization budget but can produce enough hard photons to generate some highly ionized species[45,46]. In addition, He II can also be excited by the contribution of Wolf–Rayet stars, associated with very young stellar populations (a few million years old), which would be in line with the other observational evidence for a young stellar population in the wind.

Dynamical model. We first clarify that the model shown in Fig. 4b (solid and dashed lines) is not meant by any means to be the only model that can fit the data, nor the best model. The limited information available does not allow us to discriminate among different dynamical models and between different sets of parameters within such models. The simple model shown in Fig. 4b is only meant to show that it is possible to explain the kinematics observed for the stars in a simple scenario in which stars are formed within the outflow (with an initial velocity corresponding to the gas in the outflow at that location) and then move ballistically within the galaxy gravitational potential, making them decelerate and even fall back onto the galaxy disk/bulge. Here we provide more detail about the simple model specifically used in Fig. 4b.

The gravitational potential within the central few kiloparsecs of the galaxy is supposed to follow the axisymmetric Miyamoto–Nagai disk and bulge in the form:

$$\Phi(r,z) = -\frac{GM}{\sqrt{r^2 + \left(a + \sqrt{z^2 + b^2}\right)^2}}$$

where M is the total dynamical mass of the system, G is the gravitational constant, r is the radial cylindrical coordinate on the plane of the disk, z is the coordinate perpendicular to the disk plane, and a and b are constants. The curves shown in Fig. 4b assume $M = 1.5 \times 10^{11} M_{\odot}$, where $M_{\odot}$ is the solar mass, $a = 1.7$ kpc and $b/a = 0.1$. The dynamical mass may appear somewhat large, and in particular larger than given in previous works[15]; however, one should take into account that (1) in the Miyamoto–Nagai potential the quantity M is the total mass (integrated to infinity) associated with the potential and (2) velocity projection effects make it difficult to infer a solid dynamical mass of the system, especially for nearly face-on systems (in particular the inferred dynamical mass is generally a lower limit, modulo the cosine of the inclination angle). For the sake of simplicity and for the sake of reducing the number of free parameters we have assumed that the galactic disk is oriented perpendicular to the line of sight (this is a reasonable assumption given that the rotation curve of the disk is very weak). In the model the velocity of the outflowing gas makes an angle of about 45° with the line of sight. The solid curve corresponds to particles (stars) starting from 500 pc from the nucleus (corresponding to a projected distance of about 350 pc), whereas the dashed curve corresponds to particles (stars) starting from a distance of 2 kpc from the nucleus (corresponding to a projected distance of 1.4 kpc). We emphasize that there is large degeneracy between all of these parameters and that different combinations of these parameters (as well as different gravitational potentials) can reproduce the observed stellar kinematics equally well. The locations of the arrows along the curves in Fig. 4b indicate the time intervals separated by 5 Myr.

Host galaxy disk reference velocity field. It is important to identify the reference velocity field of the (dynamically quiescent) disk of the host galaxy. As in many other studies[14,15,18,47], the narrow component of the nebular emission lines is tracing gas in the galaxy disk. The velocity field traced by the narrow component is shown in Fig. 1a and by the orange symbols in Fig. 4b, illustrating that it is relatively flat (disk probably close to face-on).

It would be useful to have also a reference for the kinematics of the stellar population in the stellar disk. This is more difficult to trace, as here we have shown that young stars are formed in the outflow and, therefore, the stellar kinematic component is probably dominated by the outflowing stars in several region. In particular, we have discussed that the stellar population traced by the Eastern part of the X-shooter slit is probably dominated by stars formed in the outflow. We have attempted to trace the stellar kinematics in other regions by exploiting the MUSE cube. This is quite difficult since both the signal-to-noise ratio and the spectral resolution of the MUSE spectra are much lower than in the X-shooter spectra. Moreover, the seeing during the MUSE observations was as bad as about 2″; this is a major issue for investigating the spatially resolved properties of the stellar population, since it implies that the strong emission from the centrally concentrated stellar population heavily contaminates the stellar light observed in the outer, fainter stellar disk, as a consequence of the wide wings of the point spread function.

Bearing in mind these various major issues, we have attempted to recover the velocity field of stars possibly not associated with the outflow and probably associated with the stellar disk, as follows. We first undertook a Voronoi binning of the MUSE cube to reach a signal-to-noise ratio higher than 35 per spectral pixel at the wavelength of the Ca II triplet. The resulting continuum flux with such a rebinning is shown in Extended Data Fig. 2a. Then we performed a PPXF fitting of the reddest line of the CaT (which is the least affected by telluric absorption) and we derived the velocity of the stellar population, which is shown in Extended Data Fig. 2b. Clearly, the stellar velocity field traced by MUSE is noisier than the X-shooter spectrum

because of the issues discussed above. Moreover, it is also clear that the MUSE data do not recover the full kinematic information obtained from the X-shooter spectra; in particular, the velocity of the stars does not reach the blueshifted values observed in X-shooter; this is clearly a consequence of the poor quality of the MUSE data: much worse seeing (Extended Data Fig. 2b), poorer spectra resolution and lower signal-to-noise. Yet the two-dimensional stellar kinematics maps show that the southern galaxy has a hint of rotation. The region towards the Northeast of the southern nucleus shows an excess of blueshifted stellar velocities, in rough agreement with the X-shooter data, modulo the higher noise and the beam smearing issues discussed above. Within all the uncertainties discussed above, the observed kinematics can be interpreted as a mild (face-on) rotation curve, with an outflowing stellar component superimposed towards the Northeast, and with everything smeared by the large seeing. We have attempted to model the rotational component by masking the northern galaxy (shaded out in Extended Data Fig. 2), by also masking the region towards the Northeast that is probably affected by the outflow and by also convolving the model with the large seeing of the MUSE observation. The resulting model is shown in Extended Data Fig. 2c.

The model should provide an indication of the stellar rotation field beneath the outflowing stars. We have extracted the inferred stellar rotation field at the same points of extraction of the X-shooter spectra. The resulting velocities are shown as green stars in Fig. 4b.

Luminosity of the Hα broad component in the outflow. Determining the absolute luminosity of the broad component of Hα is important to infer some key properties of the outflow. We focus on the regions in which the outflow is approaching (that is, the blueshifted broad component), because the receding component is more heavily affected by dust reddening, and hence affected by larger uncertainties. By selecting, in the MUSE cube, those regions where the broad component is blueshifted by more than 150 km s^{-1}, and by correcting the line flux (at each spatial position) for dust reddening as inferred by the Hα/Hβ Balmer decrement, the inferred broad line luminosity is 2.8×10^{42} erg s^{-1}. If this luminosity is used as an indicator of ionizing photons, this can be translated into a star-formation rate[27] of $15 M_{\odot}$ yr^{-1}.

By assuming a typical gas density, this luminosity can also be used to infer the mass of the warm ionized component of the outflowing gas. More specifically, the Hα luminosity $L_{\mathrm{H}\alpha}$ and the mass of ionized warm gas M_{gas} are related by the following relation[48]

$$M_{\mathrm{gas}} = 6.1 \times 10^{8} M_{\odot} \left(\frac{L_{\mathrm{H}\alpha}}{10^{44}\ \mathrm{erg\ s^{-1}}}\right)\left(\frac{\langle n_{\mathrm{e}} \rangle}{500\ \mathrm{cm^{-3}}}\right)^{-1}$$

where $\langle n_{\mathrm{e}} \rangle$ is the average electron density in the warm ionized clouds emitting Hα (where we have neglected the cloud's density contrast factor). By assuming a gas density of 500 cm^{-3}, the observed luminosity of the Hα broad component implies a mass of ionized gas in the outflow of $1.7 \times 10^{7} M_{\odot}$. However, this is a very conservative lower limit, since only a small fraction of the gas is in the warm ionized phase, while various studies have shown that the bulk of the mass is in the molecular and atomic neutral phases. According to ref. 48 the molecular phase in galactic outflows can be two orders of magnitude higher than the ionized phase. This would imply that the gas mass in the outflow of IRAS F23128−5919 could easily be higher than $10^{9} M_{\odot}$. Millimetre observations of molecular transitions are needed to properly assess the total gas mass in the outflow. We note that the quantities inferred above refer only to the approaching component of the outflow. If the receding side has similar properties, then the star-formation rate and gas mass in the whole outflow should double.

Data availability. The X-shooter observations presented in this paper were obtained through the ESO programme 293.B-5032 and the associated data are available at the ESO archive: http://archive.eso.org/cms/data-portal.html. The reduced HST, MUSE and X-shooter data that support the findings of this study (and were used to produce all figures) are available from the corresponding author upon reasonable request.

31. Cappellari, M. Improving the full spectrum fitting method: accurate convolution with Gauss–Hermite functions. *Mon. Not. R. Astron. Soc.* **466,** 798–811 (2017).
32. Sanchez-Blazquez, P. *et al.* Medium-resolution Isaac Newton Telescope library of empirical spectra. *Mon. Not. R. Astron. Soc.* **371,** 703–718 (2006).
33. Vernet, J. *et al.* X-shooter, the new wide band intermediate resolution spectrograph at the ESO Very Large Telescope. *Astron. Astrophys.* **536,** A105–A119 (2011).
34. Modigliani, A. *et al.* The X-shooter pipeline. *Proc. SPIE III*, **7737,** 773728 (2010).
35. Cardelli, J. A., Clayton, G. C. & Mathis, J. S. The relationship between infrared, optical, and ultraviolet extinction. *Astrophys. J.* **345,** 245–256 (1989).
36. Riffel, R., Rodriguez-Ardila, A. & Pastoriza, M. G. A. 0.8-2.4μm spectral atlas of active galactic nuclei. *Astron. Astrophys.* **457,** 61–70 (2006).
37. Gerardy, C. & Fesen, R. A. Near-infrared spectroscopy of the Cassiopeia A and Kepler supernova remnants. *Astron. J.* **121,** 2781–2791 (2001).
38. Garcia Lopez, R. *et al.* IR diagnostics of embedded jets: kinematics and physical characteristics of the HH46-47 jet. *Astron. Astrophys.* **511,** A5–A16 (2010).
39. Rodríguez-Ardila, A., Prieto, M. A., Portilla, J. G. & Tejeiro, M. The near-infrared coronal line spectrum of 54 nearby active galactic nuclei. *Astrophys. J.* **743,** 100–116 (2011).
40. van der Laan, T. P. R., Schinnerer, E., Böker, T. & Armus, L. Near-infrared long-slit spectra of Seyfert galaxies: gas excitation across the central kiloparsec. *Astron. Astrophys.* **560,** A99–A116 (2013).
41. Müller-Sánchez, F. *et al.* Outflows from active galactic nuclei: kinematics of the narrow-line and coronal-line regions in Seyfert galaxies. *Astrophys. J.* **739,** 69–108 (2011).
42. Maiolino, R., Krabbe, A., Thatte, N. & Genzel, R. Seyfert activity and nuclear star formation in the Circinus galaxy. *Astrophys. J.* **493,** 650–665 (1998).
43. Marconi, A., van der Werf, P. P., Moorwood, A. F. M. & Oliva, E. Infrared and visible coronal lines in NGC 1068. *Astron. Astrophys.* **315,** 335–342 (1996).
44. Piqueras López, J., Colina, L., Arribas, S., Alonso-Herrero, A. & Bedregal, A. G. VLT-SINFONI integral field spectroscopy of low-z luminous and ultraluminous infrared galaxies. I. Atlas of the 2D gas structure. *Astron. Astrophys.* **546,** A46–A83 (2012).
45. Thuan, T. X. & Izotov, Y. I. High-ionization emission in metal-deficient blue compact dwarf galaxies. *Astrophys. J.* **161** (Suppl.), 240–270 (2005).
46. Izotov, Y. I., Thuan, T. X. & Privon, G. The detection of [Ne v] emission in five blue compact dwarf galaxies. *Mon. Not. R. Astron. Soc.* **427,** 1229–1237 (2012).
47. Cresci, G. *et al.* The MAGNUM survey: positive feedback in the nuclear region of NGC 5643 suggested by MUSE. *Astron. Astrophys.* **582,** A63–A71 (2015).
48. Carniani, S. *et al.* Fast outflows and star formation quenching in quasar host galaxies. *Astron. Astrophys.* **591,** A28–A36 (2016).

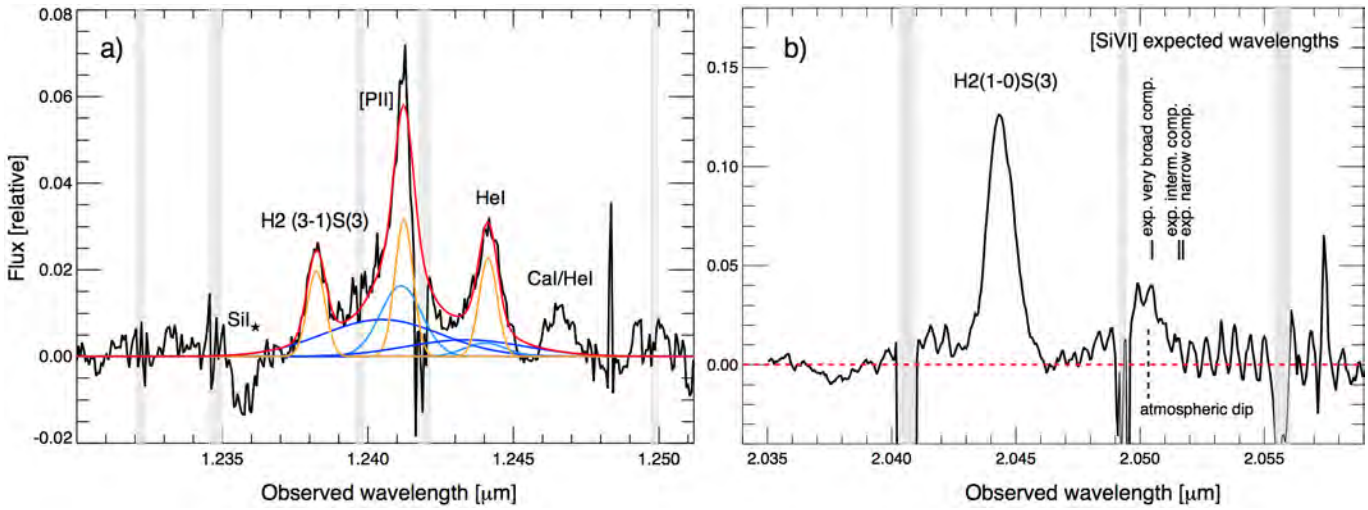

Extended Data Figure 1 | Additional sections of the near-infrared nuclear spectrum. a, Spectrum around the [P II] $\lambda = 1.188\,\mu$m line. The fitting components have the same colour coding as in Fig. 1b. **b**, Spectrum around the expected wavelength of [Si VI] at $\lambda = 1.96\,\mu$m. The expected locations of the broad and narrow components of the [Si VI] line are marked. A feature corresponding to the expected location of the broadest component is observed, but is much narrower than the width of the same component observed in other nebular lines, and is at the location of an atmospheric absorption dip.

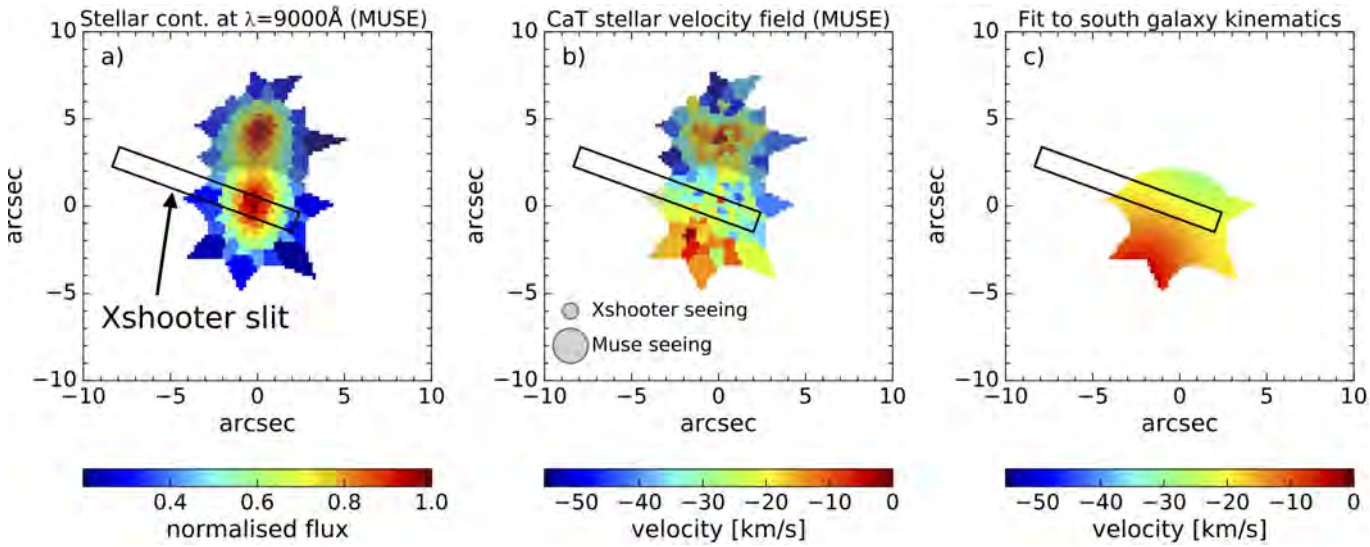

Extended Data Figure 2 | Stellar velocity field from the MUSE data. Although the quality of the MUSE data are not adequate to extract a very reliable stellar velocity field, **a** and **b** show the distribution of the stellar continuum around $\lambda = 9{,}000$ Å and the velocity field inferred from the reddest line of the Ca II triplet, by applying Voronoi binning to the MUSE cube. **b** also shows the seeing difference between the X-shooter observation and the MUSE observation. **c** shows a rotation velocity fit to the southern galaxy, by masking the region to the Northeast (around the X-shooter slit), which is probably affected by outflowing stars.